

Left atrial appendage segmentation from 3D CCTA images for occluder placement procedure



Hrvoje Leventić^{a,*}, Danilo Babin^b, Lazar Velicki^{c,d}, Daniel Devos^e, Irena Galic^a, Vladimir Zlokolica^f, Krešimir Romić^a, Aleksandra Pižurica^g

^a Faculty of Electrical Engineering, Computer Science and Information Technology, University J. J. Strossmayer Osijek, Croatia

^b imec-TELIN-IPI, Faculty of Engineering and Architecture, Ghent University, Belgium

^c Faculty of Medicine, University of Novi Sad, Serbia

^d Institute for Cardiovascular Diseases of Vojvodina, Sremska Kamenica, Serbia

^e University Hospital Ghent, Ghent University, Belgium

^f Faculty of Technical Sciences, University of Novi Sad, Serbia

^g TELIN-IPI, Faculty of Engineering and Architecture, Ghent University - imec, Belgium

ARTICLE INFO

Keywords:

Left atrial appendage
Image segmentation
Image analysis
Left atrial appendage occlusion
Left atrial appendage closure

ABSTRACT

Background: Percutaneous left atrial appendage (LAA) closure (placement of an occluder to close the appendage) is a novel procedure for stroke prevention in patients suffering from atrial fibrillation. The closure procedure planning requires accurate LAA measurements which can be obtained from computed tomography (CT) images. **Method:** We propose a novel semi-automatic LAA segmentation method from 3D coronary CT angiography (CCTA) images. The method segments the LAA, proposes the location for the occluder placement (a delineation plane between the left atrium and LAA) and calculates measurements needed for closure procedure planning. The method requires only two inputs from the user: a threshold value and a single seed point inside the LAA. Proposed location of the delineation plane can be intuitively corrected if necessary. Measurements are calculated from the segmented LAA according to the final delineation plane. **Results:** Performance of the proposed method is validated on 17 CCTA images, manually segmented by two medical doctors. We achieve the average dice coefficient overlap of 92.52% and 91.63% against the ground truth segmentations. The average dice coefficient overlap between the two ground truth segmentations is 92.66%. Our proposed LAA orifice localization is evaluated against the desired location of the LAA orifice determined by the expert. The average distance between our proposed location and the desired location is 2.51 mm. **Conclusion:** Segmentation results show high correspondence to the ground truth segmentations. The occluder placement method shows high accuracy which indicates potential in clinical procedure planning.

1. Introduction

Survey performed by World Health Organization [1] has identified stroke as the second leading global cause of death with over 6 million deaths in 2015. The risk of stroke drastically increases in patients suffering from atrial fibrillation (AF) [2]. With atrial fibrillation, the normal regular rhythm of the heart becomes irregular, due to disorganized electrical signals in the upper heart chambers, called the atria. This chaotic electrical activity causes asynchronous contractions of the atria, which do not allow the heart chambers to fill and empty properly. Without effective blood pumping, the blood can sometimes pool in the heart and form a blood clot, i.e. thrombus, and it is this

clotting that increases the risk of a stroke. Pieces can break off from a clot, forming thromboemboli, which can be passed from one chamber to the next and then end up in the brain arteries causing a stroke. Atrial fibrillation is a cardiac disease shown to be responsible for almost 20% of all strokes [3] and the majority of cardioembolic strokes [2]. The vast majority of cardioembolic strokes are the result of cardiac thromboemboli formed in the LAA [4,5]. Estimates show that over 33 million people worldwide suffer from atrial fibrillation [6].

Left atrial appendage closure is a stroke prevention method for patients with AF [7]. The closure procedure demonstrated non-inferiority to anticoagulation therapy for stroke prevention [8,9] while avoiding most of the contraindications associated with the antic-

* Corresponding author.

E-mail address: hrvoje.leventic@ferit.hr (H. Leventić).

oagulation therapy. The procedure is performed by percutaneously deploying the occluder device to the neck of the LAA and stopping the blood flow between left atrium (LA) and LAA, thus preventing the formed thrombi from leaving the LAA and causing stroke. Closure devices are available in several predefined sizes and for each patient an appropriately sized device has to be selected. Selection of the correct size of the occluder requires accurate measurements of the LAA. Coronary CT angiography images (CCTA) have shown to be superior to other imaging modalities [10–13]. The work of [13] presents the complete list of anatomic and imaging landmarks that determine the feasibility of closure procedure. The most important measurements for correct occluder placement are: diameter (circumference) of the orifice, shape of the orifice, LAA volume and type of the LAA morphology. These measurements can be accurately performed using CCTA image segmentation, analysis and visualization.

Vast majority of LAA segmentation and analysis studies determine the required anatomical measurements manually. Two most often used approaches are: manual measurements directly from original images [10] and measurements from manually segmented 3D volume [14,15]. Manual 3D segmentation is a time-consuming and error prone process, where segmentation is performed slice-by-slice with a paintbrush tool [15]. Additionally, 3D segmentation can be performed using interactive guided segmentation methods. Such methods improve the segmentation speed but still require time for manual corrections of segmentation leaks [14]. The standard region growing methods for guided interactive segmentation all suffer from segmentation leaks due to the inhomogeneous distribution of contrast agent in the appendage and proximity of highly-contrasted surrounding vessels. In other words, a threshold value that will accurately isolate the LAA region (so that no surrounding structures are included) will consequently result in an under-segmented LAA. On the other hand, a threshold value that will allow for the whole LAA region to be segmented, will also produce an over-segmentation due to leaks to surrounding structures. Most of the user-guided methods use some kind of thresholding to guide region growing. Geodesic active contours [16], implemented in ITK-SNAP [17], use the speed image (often created using thresholding) for guiding the contour evolution process. Even with methods that can generally avoid segmentation leaks by using multi-scale voxel properties (such as generalized pixel profiling [18] and line-shaped profiling [19]), the delineation between the appendage and the atrium remains to be determined from anatomical properties.

To the best of our knowledge, there are only few automatic and semi-automatic LAA analysis and segmentation methods. The method proposed in Ref. [20] uses a multi-part based approach to automatically segment the left atrium, including the LAA and the pulmonary veins (PV). Individual models are fitted using marginal space learning and later merged into a consolidated mesh. Their second algorithm [21] is also based on multi-part based approach using marginal space learning, but in this approach the segmentation refinement is performed using region growing based on adaptive thresholds, followed by removal of the leakage using graph cuts.

The method proposed in Ref. [22] is an improvement of the method from Ref. [23] and requires manual selection of four seed points to obtain LAA bounding box representing the ROI. The method segments the LAA from each 2D slice in the ROI using fully convolutional neural networks. Afterwards, all 2D segmentations are refined and merged into a 3D model using modified 3D convolutional random fields. The same group proposed the method for the LAA neck modeling in CCTA images [24] based on LAA segmentation obtained by method in Ref. [23]. The method of [25] performs segmentation of 4D CT LAA images for diagnosis of atrial fibrillation using parametric max-flow method and graph-cut approach to build 3-D model of each time instance of the sequence. Methods [26,27] adapt the input to a predefined model of the

heart to locate the LAA, which is used as an input for deformable models (guided by minimizing external and internal energy) to fit the exact shape of the appendage. The model-based approach was used also in Refs. [28,29], but with an aim of whole heart segmentation, where segmented LAA was only a side result. The main challenge with the machine learning based methods (such as the methods described above) is the reproducibility of the results without access to the training datasets. Our earlier work on semi-automatic segmentation of left atrial appendage [30] required selection of a threshold value and two seed points (one inside the LAA and another inside LA), while the orifice was manually determined by selecting three points forming the delineation plane.

We propose in this paper a semi-automatic LAA segmentation method that requires only one input threshold value and selection of a seed point (the LA is localized automatically). The method is robust to threshold value selection and segmentation leaks. The resulting binary image is used for all subsequent steps. Our method performs the detection of centerline connecting the seed point and the center of the left atrium. Segmentation of LAA and LA is accomplished using the detected centerline. The occluder placement localization is performed by detecting the plane separating the LAA from the LA at local diameter minima and presenting it to the user. User can accept or modify the proposed delineation plane between LAA and LA. The final segmentation refinement is performed with respect to the selected delineation plane. Our method calculates the orifice diameter and circumference together with LAA volume according to the final delineation plane. The orifice shape and LAA morphology type are easily determined from the visualized segmentation.

The main advantage of the proposed method is the invariance to the type and dimensions of the binary image used for subsequent segmentation steps. Any type of binary image can be used as an input to the method (e.g. binary images created with active contours, or images from MRI), as long as the input binary image contains the LAA and most of the left atrium.

2. Proposed method

In this paper we propose a novel method for segmentation and analysis of left atrial appendage from CCTA images. The segmentation is performed using only two inputs: an initial threshold value and a seed point placed inside the LAA. The method proposes the occluder placement location based on the local diameter minima of the orifice and calculates the parameters needed for planning of the closure procedure. The proposed method consists of the following steps (see Fig. 1):

1. Thresholding is used to produce a mask image which contains leaks (due to over-segmentation) and which will be refined in the subsequent steps. The mask image is also used for computation speed-up.
2. Euclidean distance transform (EDT) is used to produce EDT image from the thresholded (mask) image. The EDT image will be used to determine the LAA centerline and to refine the segmentation while avoiding the leaks contained in the mask image.
3. Centerline is calculated by tracking the largest radii values in the EDT image starting from the seed point in the LAA to the center of the LA (which is automatically detected). The initial segmentation is obtained by reconstructing the LAA volume from the obtained centerline and the mask image (fitting the maximum radii spheres at each centerline position). The initial segmentation is further refined by adding border regions with decreasing radii values in the EDT image (increase in values indicates presence of leaks, in which case the adding is stopped).
4. Localization of the LAA neck and orifice is performed by searching

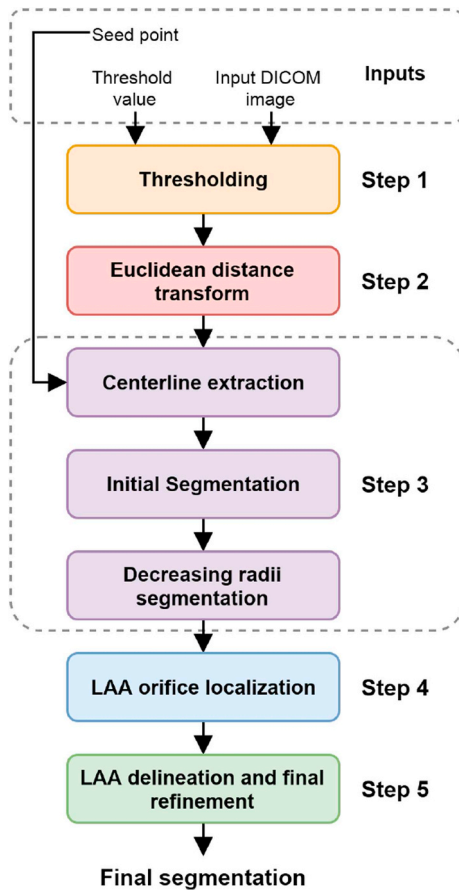


Fig. 1. Proposed method flow diagram.

the local segmented LAA diameter minima while taking into account the increase in diameter values (as a way of detecting the atrium). 5. The final segmentation refinement is based on the determined orifice location. Isolated connected components adjacent to the segmented LAA, which are of smaller volume than the existing segmentation, are added to the final result.

2.1. Threshold selection

In this subsection we explain the effects of threshold selection on the overall method. The user selects the threshold value by visual inspection of the LAA in CCTA image slices. The selected threshold value will result in a mask image with approximate over-segmentation of the contrasted blood in the input CCTA images. Care should be taken to select the threshold value in such a manner that will enable the segmentation of the contrasted blood inside the heart, while preventing the segmentation of the heart muscle. Because of vast differences in shape, size and location of LAA in the heart it is possible that after thresholding the appendage appears connected to other anatomical structures, most often one of pulmonary veins. If the threshold value is too high, resulting segmentation will be under-segmented (compared to the ground truth). If the threshold is too low, over-segmentation occurs and leaks become a significant problem for most segmentation algorithms. We emphasize at this point that threshold value is used only to produce a mask as a further input for our method. The subsequent steps of our method are robust to over-segmented mask image and are designed to deal with segmentation leaks.

2.2. Euclidean distance transform

We calculate the Euclidean distance transform (EDT) image from the thresholded (mask) image using the Euclidean distance transform. The EDT image will be used to extract the centerline of the appendage and to refine the segmentation while avoiding segmentation leaks. Let B be the set of all background voxels \mathbf{v}_B in the mask image. The value of each voxel $\mathbf{v} \in Z^3$ in the EDT image will be:

$$r(\mathbf{v}) = \begin{cases} \min(d(\mathbf{v}, \mathbf{v}_B)); & \mathbf{v} \notin B \\ 0; & \text{otherwise} \end{cases} \quad (1)$$

where $d(\mathbf{v}, \mathbf{v}_B)$ is the Euclidean distance between voxels \mathbf{v} and \mathbf{v}_B . For a given voxel \mathbf{v} , the intensity value in the EDT image ($r(\mathbf{v})$ – the distance to the nearest background voxel in the mask image) is actually the radius of the largest sphere (centered in the voxel \mathbf{v}) inscribed in the mask image (such that no voxels in the sphere touch the background). All subsequent steps in the proposed method are based on finding spheres of certain radii using the values calculated in this step. Calculation of EDT image improves performance of the method because the radius of each needed sphere can be determined by a simple lookup from EDT image. For performance reasons, our method uses Maurer Distance Map method [31] generalized to N-dimensional spaces implemented inside SimpleITK framework [32].

2.3. Centerline extraction

In this subsection we propose a method for centerline detection which is later used for obtaining the initial segmentation and to determine the optimal occluder placement location. The purpose of the proposed centerline detection method is to find a path along the largest radii from seed point in the appendage to the center of the atrium. The centerline detection method consists of the following steps:

1. Tracking the highest radii values in the EDT image from a user defined seed point to the center of the atrium
2. Extraction of the centerline from the tracked highest radii path.

The final result of the method is an ordered set of voxels from the seed point to the center of the LA.

2.3.1. Tracking maximum radii voxels

The idea behind tracking the maximum radii voxels is to produce a centerline (skeleton) that will connect the user-defined seed point with the center of the atrium along the most likely path (the path with the highest radii values along the way). Let $S(\mathbf{v})$ be a set of voxels belonging to the maximum inscribed sphere in the mask image centered at voxel $\mathbf{v} \in Z^3$:

$$S(\mathbf{v}) = \{\mathbf{q} \in Z^3 \mid d(\mathbf{v}, \mathbf{q}) \leq r(\mathbf{v})\}, \quad (2)$$

where $r(\mathbf{v})$ is a radius of the maximum inscribed sphere contained in the EDT image, as defined in (1). The tracking is performed by iteratively searching for the voxel with the largest radius in a set of voxels P . In search set P we locate the voxel with the largest value in the EDT image:

$$\mathbf{v}_{\text{rmax}} = \arg \max_{\mathbf{v} \in P} r(\mathbf{v}), \quad (3)$$

and we add it to the output set of tracked maximum radii voxels T . In the initial iteration the set T is an empty set. Along with adding \mathbf{v}_{rmax} to T , we also add the set of voxels $L(\mathbf{v}_{\text{prev}}, \mathbf{v}_{\text{rmax}})$ representing the voxels on the line segment between the maximum radii voxels in the previous and current iteration. The algorithm is described in Algorithm 1.

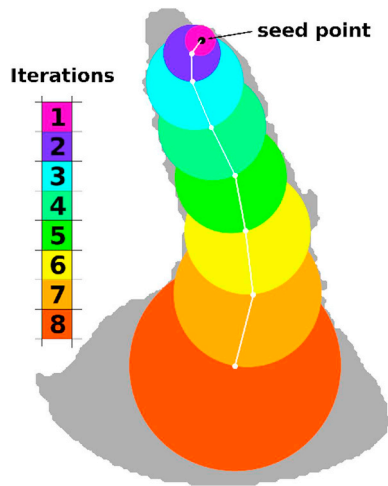


Fig. 2. Centerline tracking by iterative selection of maximum radii voxels in the largest inscribed spherical neighborhood.

Algorithm 1. Tracking maximum radii voxels algorithm.

$$P = S(\mathbf{v}_{seed}) \text{ according to (2)}$$

for $i = 1$ to n **do**

$$\mathbf{v}_{prev} \leftarrow \mathbf{v}_{rmax}$$

Find \mathbf{v}_{rmax} in P according to (3)

Append \mathbf{v}_{rmax} to T

Append $L(\mathbf{v}_{prev}, \mathbf{v}_{rmax})$ to T

Append $S(\mathbf{v}_{rmax})$ to P

end for

The general idea behind the proposed algorithm is illustrated in Fig. 2. The gray area in the image illustrates a masked LAA region. Each colored circle in the figure represents a sphere in 3D space, while white dots represent the selected voxels \mathbf{v}_{rmax} in each iteration (color coding of iterations is given on the left side of the figure). The initial search set P in Fig. 2 is illustrated by the circle (representing a sphere in 3D) generated in the first iteration (color code 1). In the given set, the maximum radius voxel \mathbf{v}_{rmax} is found (in this case on the border of the initial sphere) and added to the output set T (along with the voxels on the line connecting the previously added voxel and the newly added voxel). The search set P is extended by the maximum inscribed sphere voxel set of the newly added voxel $S(\mathbf{v}_{rmax})$. This means that the search set P has grown and includes largest inscribed spheres from the first 2 iterations (color codes 1 and 2). The above principle is repeated until the tracking reaches the center of the atrium. In fact, the above iterations are repeated in a pre-defined number of steps (calculated from the image size, image spacing and expected anatomical properties of LAA) in which we are certain that the output set T will contain voxels from the central part of the atrium (for further explanation refer to Section 4).

The width of the LAA along the centerline is almost never consistently increasing (as illustrated in Fig. 2). The anatomy of the LAA along the centerline will interchangeably get wider and narrower until the centerline reaches the left atrium (see the result of the maximum radii voxel tracking in Fig. 3b). When the algorithm reaches a widening in the anatomy it will iteratively add to the output T all the large radius voxels in the widening until the voxel with the largest radius becomes the voxel that will continue along the path towards the left atrium, as illustrated in Fig. 3a. If the LAA has a widening near the tip and the

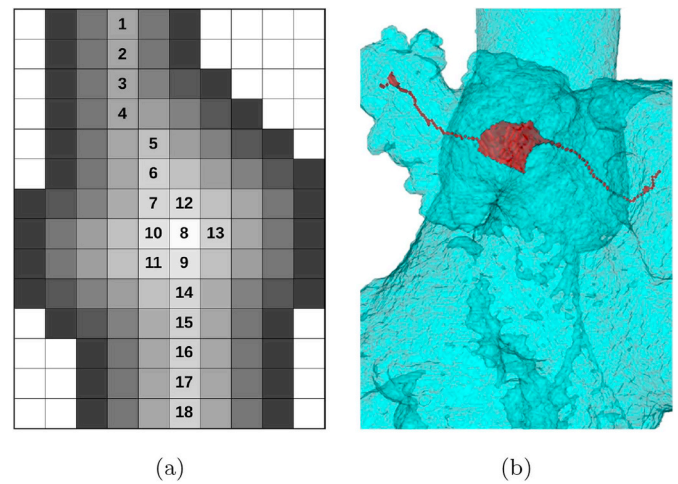


Fig. 3. Example of a widening in the anatomy during the maximum radii tracking. (a) Illustration of the order of voxels added to the tracked maximum voxel radii, where pixel gray value represents the radius value. (b) Example of tracked maximum radii voxels (red) visualized with its corresponding LAA mask (blue).

algorithm starts to move the path towards the tip of the LAA, once it has added all the largest radii in that widening it will inevitably move back to the correct direction (towards the atrium). Fig. 3b illustrates the voxels added to the centerline path from seed point to the maximum radius point in the LA (which we define as the center of the LA).

2.3.2. Centerline extraction

Tracking of maximum radii voxels resulted in a set of voxels T connecting the user-defined seed point and the center of the atrium. However, the set T does not represent a centerline path, which we need for further analysis. Therefore, in this subsection we will perform skeletonization and longest path extraction from the maximum radii voxels set T based on our earlier work [33].

Ordered skeletonization [33] is the process of iterative thinning of a binary image. The thinning is performed by discarding the voxels in a predefined order. The goal is to obtain a one-voxel wide centerline from the input image. The ordered skeletonization process consists of the following steps:

- Calculation of the distance transform from the input image.
- Sorting of voxels into an ascending distance value ordered list.
- Iterating through the list to discard the redundant voxels according to voxel redundancy criteria proposed in Ref. [33] until it results in one-voxel wide centerlines.

The result of the ordered skeletonization is a skeleton as a set of voxels forming a one-voxel wide connected component from seed point to the LA center. However, the resulting skeleton also contains stubs and multiple paths which are a byproduct of the skeletonization process, as visible in Fig. 4a. Next, we represent the skeleton as a simple graph, where every foreground voxel in the skeleton is a graph node. Let \mathbf{v}_1 be the node with the largest shortest path distance [34] from the seed point node. Let \mathbf{v}_2 be the node with the largest shortest path distance from \mathbf{v}_1 . The centerline C is an ordered set of voxels in the shortest path from \mathbf{v}_2 to \mathbf{v}_1 . The first voxel in C is either a seed point or a voxel very close to the seed point. The last voxel in C represents the center of the LA. Fig. 4b shows an example of an extracted centerline.

2.4. Initial segmentation

In this subsection we explain how the initial segmentation is created which is used as a starting LAA segmentation to be refined with the

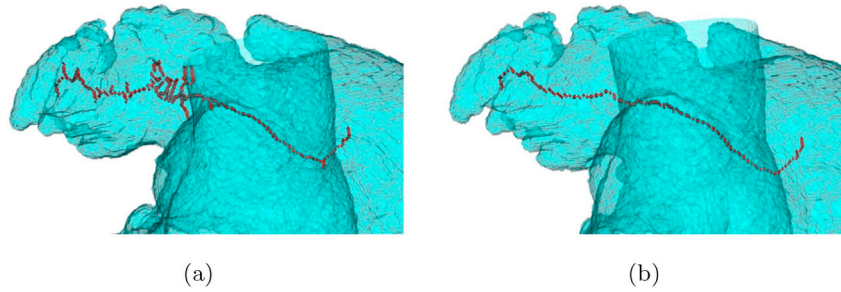


Fig. 4. Steps in centerline extraction method. (a) Result of the ordered skeletonization applied to the set of tracked maximum radii voxels T . (b) The extracted longest path (without loops) of the skeleton is the final LAA centerline result.

Decreasing radii segmentation described in section 2.5. Creation of the initial segmentation is based on the EDT image and the set of tracked maximum radii voxels T , which represents a set of voxels in the path from the seed point to the center of LA, as described in 2.3.1. We create the initial segmentation by adding the spheres of all voxels in T to the initial segmentation image:

$$I = \bigcup_{\mathbf{v} \in T} S(\mathbf{v}). \quad (4)$$

Left side of Fig. 5 shows the centerline path C and the resulting initial segmentation along the given centerline.

2.5. Decreasing radii segmentation algorithm

In this subsection we propose a novel method for leak resistant segmentation based on the initial LAA segmentation. Decreasing radii segmentation is based on iterative addition of spherical voxel neighborhoods to the existing segmentation. The addition of neighborhoods is done for the regions where the LAA anatomy is shrinking, which is indicated by decreasing radii of the spherical neighborhoods. The regions with increasing radii are regions of leaks, and are not added to the segmentation. Left side of Fig. 5 shows an initial segmentation with the computed centerline. The right side of Fig. 5 shows the decreasing radii segmentation of iterative spherical neighborhood addition. Smaller segments of anatomy are added to the existing segmentation in each iteration (the initial segmentation is shown in red and each additional iteration is shown in different color). For visualization purposes the segmentation in Fig. 5 is limited to 6 iterations. Explanation of the decreasing radii segmentation method follows.

Let H^i denote a set of all segmented voxels in an iteration i (the segmentation set in first iteration will contain only the voxels from the initial segmentation $H^1 = I$). Let $N_{26}(\mathbf{v})$ be the 26-neighborhood of

voxel \mathbf{v} . We define a set of voxels on the edge (boundary) of the current segmentation set H^i as:

$$E^i = \{\mathbf{v} \in H^i \mid \exists \mathbf{q} \in N_{26}(\mathbf{v}), \mathbf{q} \notin H^i\}. \quad (5)$$

Let us denote the set of unsegmented voxels (those that do not belong to the set of the segmented voxels H^i) centered at voxel \mathbf{v} within the maximum inscribed sphere $S(\mathbf{v})$ with:

$$U^i(\mathbf{v}) = \{\mathbf{q} \mid \mathbf{q} \in S(\mathbf{v}), \mathbf{v} \in H^i, \mathbf{q} \notin H^i\}, \quad (6)$$

For every edge voxel $\mathbf{v} \in E^i$ we add to segmentation H^i all unsegmented voxels inside its sphere $U^i(\mathbf{v})$ if the radii of all those voxels in $U^i(\mathbf{v})$ are smaller or equal to the maximum radius value of the given voxel $r(\mathbf{v})$:

$$A^i(\mathbf{v}) = \begin{cases} U^i(\mathbf{v}) & ; \forall \mathbf{q} \in U^i(\mathbf{v}), r(\mathbf{q}) \leq r(\mathbf{v}) \\ \emptyset & ; \text{otherwise} \end{cases} \quad (7)$$

$$A^i = \bigcup_{\mathbf{v} \in E^i} A^i(\mathbf{v}). \quad (8)$$

Voxels A^i are added to the segmentation for the next iteration:

$$H^{i+1} = H^i \cup A^i. \quad (9)$$

The algorithm stops when no new voxels were added to segmentation in an iteration, i.e. when $H^{i+1} = H^i$.

Fig. 6a shows an example of a voxel on the segmentation boundary (green) and a sphere to be added. The voxel at the center of the sphere (green) has the radius value 7, while all the other voxels in the unsegmented part of the sphere have a radius that is smaller than 7. This sphere will be added to segmentation. Fig. 6b shows an example of a sphere which will not be added to segmentation. The voxel at the center of the sphere (red) has the radius of 7, but in this case there are voxels in the unsegmented part of the sphere which have a radius value larger than 7 (shown in red). Fig. 7 illustrates robustness of the method to segmentation leaks. As long as the width of the anatomical structure (into which the segmentation is leaking) is wider than the width of the leak itself, the decreasing radii segmentation will not leak into that structure, because the radii values of voxels inside that structure will be larger than the radii of the voxels inside the leak.

2.6. Detection of LAA orifice

In this subsection we propose a novel method for the detection of the LAA orifice which is considered to be the location for the occluder placement and as the delineation position between the LAA and LA. According to [35] the orifice is defined as the narrowest part of the LAA neck. Therefore, in order to locate the orifice we propose to search for the narrowest part of the LAA neck along the centerline. The narrowest part of the appendage neck will be a location with a local minimum in calculated cross-sectional area. On the other hand, the neck is a part of the appendage proximal to the highest growth in the cross-sectional area (the area along the centerline rapidly increases as we pass from the appendage to the atrium [36]). The method measures cross-sectional

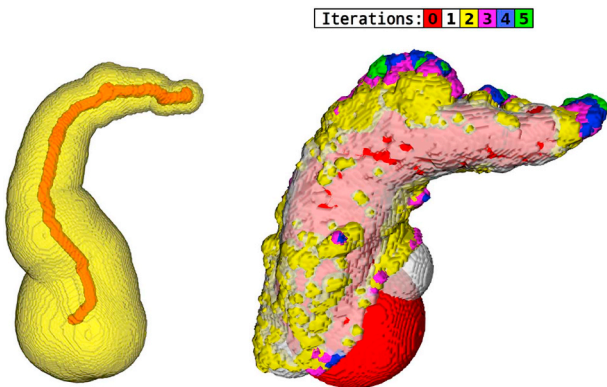


Fig. 5. Illustration of Decreasing radii segmentation algorithm. Left: the initial segmentation is created from the extracted centerline by morphological reconstruction using maximal inscribed spheres. Right: connected components colored according to the iteration in which they were added to the segmentation result in the decreasing radii segmentation method.

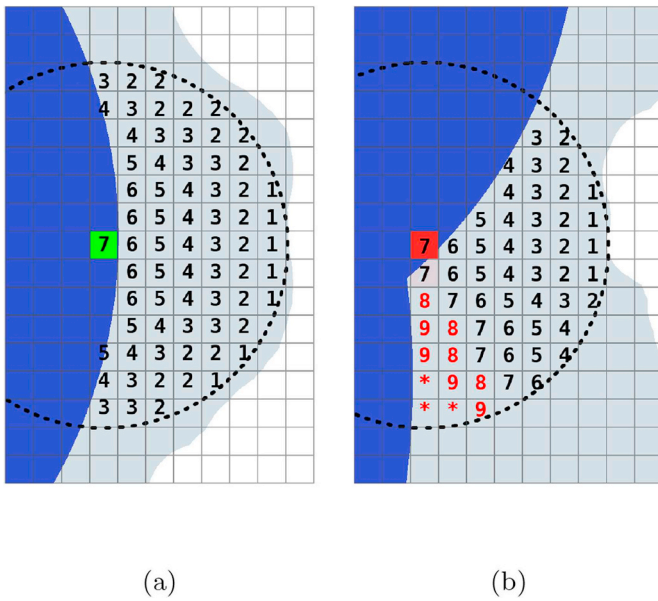


Fig. 6. Illustration of the decreasing radii segmentation principle. (a) Voxels in the spherical neighborhood of the current voxel will be added to the segmentation because all of them have the radius value lower than the radius value of the current voxel. (b) None of the voxels in the spherical neighborhood of the current voxel will be added to the segmentation because some of them have the radius value higher than the radius value of the current voxel.

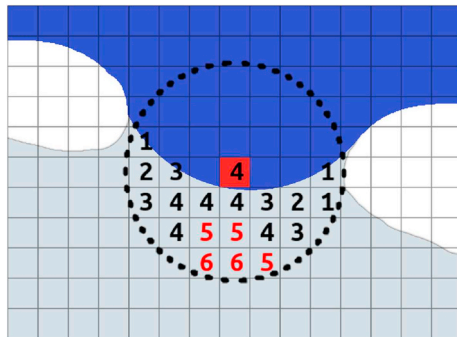


Fig. 7. Segmentation leaks are characterized as regions in which the values of maximum radii increase. Because of this, the decreasing radii segmentation method will prevent the leak regions from being added to the segmentation.

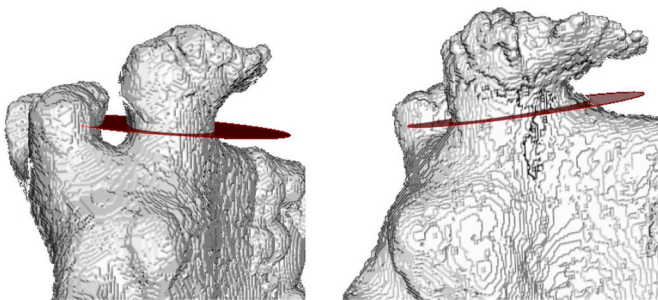


Fig. 8. Example of the proposed LAA orifice location and its cross-sectional plane of minimum area.

areas along the centerline to find the local minima and the highest growth in cross-sectional area. Fig. 8 shows the calculated orifice location with the cross-sectional plane of the minimum area. Proposed orifice detection algorithm consists of two steps: (1) calculation of the areas along the centerline C and (2) search for the smallest area within calculated areas which occurs right before the LA.

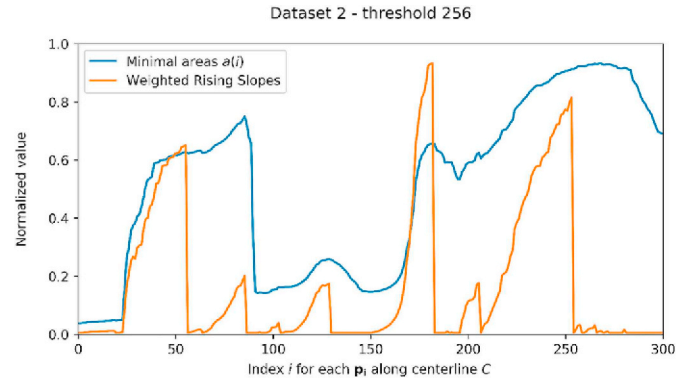


Fig. 9. Plot of minimal areas and weighted rising slopes along the centerline. The maximum of the weighted rising slopes indicates the position (on the centerline) of the LAA orifice.

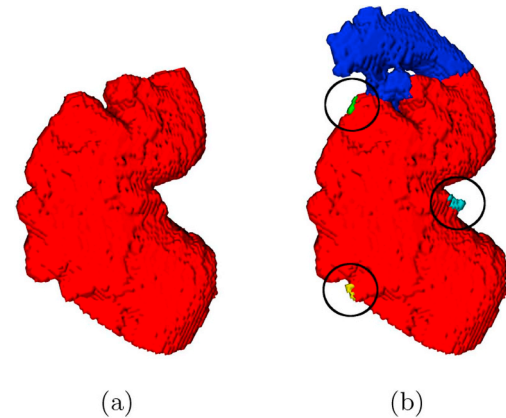


Fig. 10. Isolated connected components which are smaller than the segmented LAA are added to the segmentation result in the segmentation refinement step. (a) Segmentation result before the refinement (after decreasing radii segmentation and orifice localization). (b) Segmentation result after the refinement step.

Let $\mathbf{p}(i)$ denote a position on the LAA centerline C with index i . For each position $\mathbf{p}(i)$ we calculate the normal vector $\mathbf{n}(i)$ for the cross-sectional plane:

$$\mathbf{n}(i) = \mathbf{p}(i + 1) - \mathbf{p}(i - 1). \tag{10}$$

Therefore, the cross-sectional plane $\psi(i)$ is defined by the position $\mathbf{p}(i)$ along the centerline and the normal $\mathbf{n}(i)$. Let us denote the area of the centerline cross-section at position $\mathbf{p}(i)$ with $a(i)$. The cross-sectional area $a(i)$ will be the area of the region defined by the intersection of the discrete positions of the plane $\psi(i)$ and the segmentation set H :

$$a(i) = |D(\psi(i)) \cap H|, \tag{11}$$

where $D(\psi(i))$ denotes the set of discretized positions of plane $\psi(i)$.

In some cases, the cross-sectional plane (defined by the normal $\mathbf{n}(i)$) will not accurately represent the minimum cross-sectional area of the appendage at the given centerline position. This happens because the centerline does not necessarily represent the variations in shape of LAA edges. To surpass this problem, we search for the minimum cross-sectional area plane by testing a number of planes with different normals (not only the plane perpendicular to the centerline direction). The planes are created by modifying the normal $\mathbf{n}(i)$ up to 40 degrees (determined experimentally) and the full circle rotation. The final area $a(i)$ is the minimum area calculated from the candidate cross-sections. The plot of minimal areas along the centerline $a(i)$ is illustrated in Fig. 9.

As explained earlier, the location of the orifice is defined as the

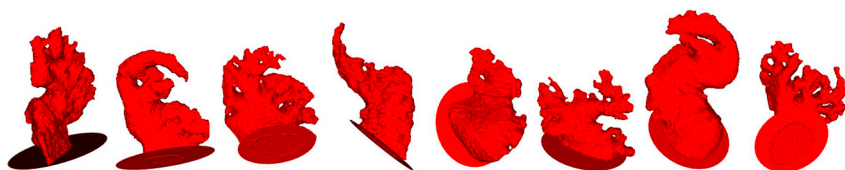


Fig. 11. Examples of LAA segmentation results.

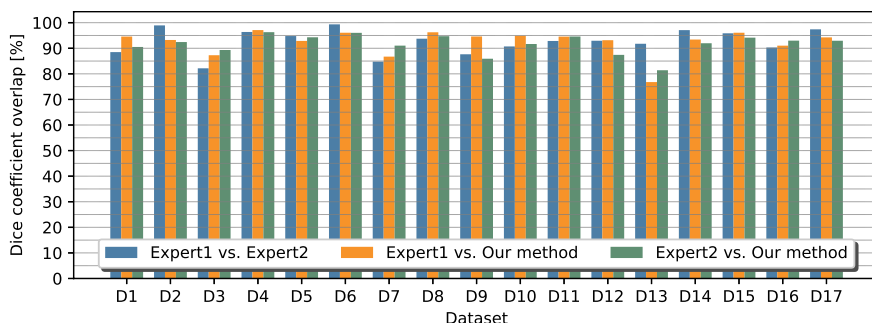


Fig. 12. Plot of dice coefficients overlap.

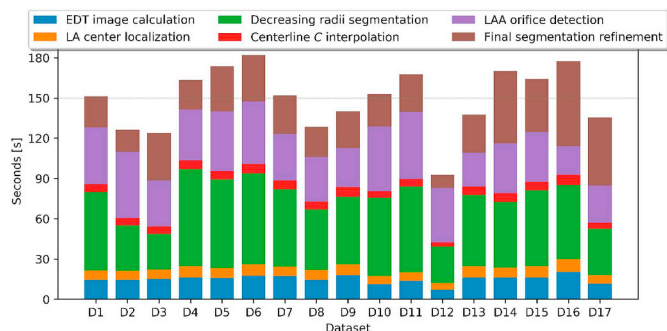


Fig. 13. Execution runtime of proposed method in each dataset. We use different color code for each step.

narrowest position in the neck of the LAA, while the neck represents the part of the appendage just in front of the atrium. Hence, we need to find the local minima and the highest growth in the cross-sectional area $a(i)$. The highest growth in cross-sectional area also has to be the most dominant one in its surrounding to account for growth of cross-sectional area due to LAA shape. For this reason we introduce weighted rising slopes $w(i)$ representing the rate of change in minimal area $a(i)$ along the centerline C (depicted in Fig. 9 with orange line). On intervals where $a(i)$ is decreasing the function $w(i)$ is set to zero. Within the intervals where $a(i)$ is increasing let $m(i)$ be the index of the closest local minimum to index i . We calculate $w(i)$ in the following way:

$$w(i) = \sqrt{(m(i) - i)^2 + (a(m(i)) - a(i))^2}. \tag{12}$$

Peaks of $w(i)$ represent locations where the $a(i)$ along the centerline C had the largest uninterrupted increase. These locations are potentially inside the LA. The last location where $w(i) = 0$ before the largest peak in $w(i)$ is the location of the last narrowing of the anatomy before the largest increase in the calculated areas (widening of the anatomy) and represents the proposed location of the orifice. According to (12) it is evident that the value of $w(i)$ increases with the length of uninterrupted growth in area values along the centerline. Proposed location of the orifice for the dataset in Figs. 8 and 9 is at the location of $i = 140$ and shown in Fig. 8 as red plane. However, observing Fig. 9 we can see a large peak at $i = 51$. At this point the centerline is still inside the LAA. We want to penalize the peaks occurring within the LAA to make sure that the largest peak will be inside the LA. Let the $w_r(i)$ be another discrete function called *radius weighted rising slopes*, and let the $r(i)$ be the radius of the voxel from EDT image at location i . In this case the

$w_r(i)$ is as follows:

$$w_r(i) = w(i) \cdot r(i) \tag{13}$$

Radius values from EDT image will be small inside the LAA and large inside the LA. Multiplying the weighted rising slope values by radius value ensures that even if the calculated area inside LAA gets very large, the resulting weights will still be smaller within the LAA and larger inside the LA. Fig. 14 shows 3 datasets with calculated $w_r(i)$ and proposed orifice locations.

2.7. Segmentation refinement

The final refinement of the LAA segmentation deducts the obtained LAA segmentation from the mask segmentation (thresholded image) and labels all isolated connected components. Some connected components will be adjacent to the segmented component and will represent small parts of the LAA not previously added to the LAA segmentation. We create the final LAA segmentation by adding to the segmentation all components directly connected to LAA component with the volume smaller than the volume of the LAA component. Fig. 10 shows the segmentation result before and after the refinement step with four isolated components which were not originally segmented with decreasing radii segmentation, but were added to the segmentation in the refinement step. The largest component is shown in blue, while the other three smaller components are emphasized with black circles.

3. Results

The evaluation dataset contains 17 (3D and 4D) CCTA images of patients suffering from cardiovascular diseases. All patients have given their written consent for the use of their images in this research. The patient population properties are given in Table 1. The images were acquired using a Siemens Somatom 64-slice scanner for the purpose of Coronary CT Angiography. To obtain the ground truth segmentation, each of the 17 datasets was manually segmented by two medical experts: a radiologist and a cardiovascular surgeon. Doctors manually determined the threshold, segmented the LAA by guiding the Geodesic active contours segmentation in ITK-SNAP [17] and corrected the resulting segmentation with a paintbrush tool. Twelve out of 17 datasets had significant leaks during the guided segmentation part and extensive corrections using the paintbrush tool were necessary. Average duration of the segmentation per image was approximately 10 min, with the shortest segmentation requiring 5 min and the longest 17 min.

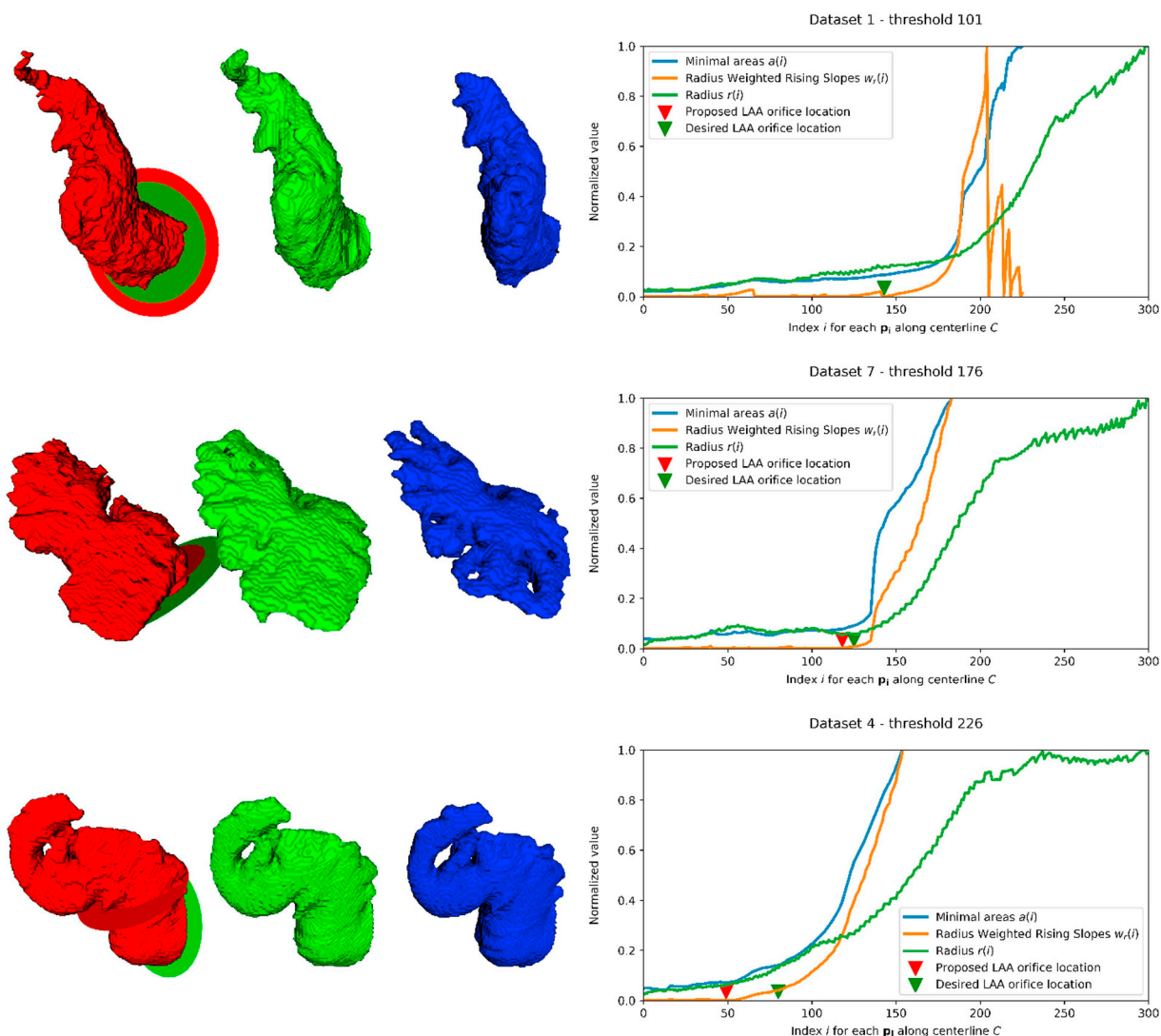


Fig. 14. Segmentation results on 3 selected datasets. From left to right: our segmentation result (red), manual segmentation by the first expert (blue), manual segmentation by the second expert (green), plot of radius weighted rising slopes (on the right) and LAA delineation plane p_i positions (our proposal in red and desired delineation plane in green).

Table 1
Validation dataset (17 patients).

	N	%
Patient age		
Under 35	3	17.65%
35 - 44	2	11.76%
45 - 54	2	11.76%
55 - 64	6	35.29%
65 and older	4	24.53%
Patient gender		
Male	6	35.29%
Female	11	64.71%

Visualizations of several datasets segmented with the proposed method are presented in Fig. 11. Our segmentation results are evaluated by dice similarity coefficient overlap with each of the two validation datasets created by two medical experts. Our method achieves the average dice coefficient overlap of 92.52% and 91.63% against the ground truth segmentations. The average dice coefficient overlap between the two ground truth segmentations is 92.66%. Results of the orifice localization and minimum area cross-sectional plane placement are shown in Fig. 8. Our proposed LAA orifice localization is evaluated

Table 2
Dice coefficients overlap (n = 17). Table shows dice overlap between segmentations of our two experts (E1, E2) and the overlap of segmentation results with our method between each of the experts' segmentations.

Dataset	dice (E1, E2)	dice (E1, our)	dice (E2, our)
D1	88.50%	94.58%	90.51%
D2	98.94%	93.24%	92.43%
D3	82.16%	87.28%	89.32%
D4	96.37%	97.11%	96.29%
D5	94.78%	92.87%	94.29%
D6	99.35%	96.07%	96.03%
D7	84.77%	86.73%	91.03%
D8	93.74%	96.25%	94.72%
D9	87.65%	94.61%	85.91%
D10	90.71%	94.90%	91.66%
D11	92.85%	94.56%	94.60%
D12	92.94%	93.15%	87.42%
D13	91.76%	76.78%	81.41%
D14	97.09%	93.41%	91.96%
D15	95.85%	96.07%	94.15%
D16	90.30%	91.02%	92.98%
D17	97.40%	94.25%	92.94%
Avg:	92.66%	92.52%	91.63%

Table 3

Distance in mm between center points of our proposed location for LAA orifice and the desired location determined by medical expert.

Dataset	Distance in mm
D1	0.00 mm
D2	1.07 mm
D3	5.84 mm
D4	9.70 mm
D5	0.53 mm
D6	0.18 mm
D7	1.62 mm
D8	0.65 mm
D9	4.04 mm
D10	7.54 mm
D11	0.50 mm
D12	0.67 mm
D13	0.57 mm
D14	1.25 mm
D15	0.00 mm
D16	5.52 mm
D17	3.07 mm
Avg:	2.51 mm

against the desired location of the LAA orifice determined by the expert. The average distance between our proposed location and the desired location is 2.51 mm.

The average runtime of our proposed segmentation method on our datasets is two and a half minutes (149 s on Intel i7, 4.3 GHz, 16 GB RAM). The runtime depends on the size of the input dataset, as well as the anatomy of the patient in the dataset. The execution runtimes for each dataset are presented in Fig. 13, where each step in the method is shown with different color. Our method obtains clinically acceptable results.

The delineation according to the calculated orifice location is performed for both our segmentation and the ground truth expert segmentations. Table 2 shows the dice coefficient overlaps for each dataset. Dice overlaps are also shown in Fig. 12 for easier visualization. Table 3 presents the distances in mm between our proposed LAA orifice location and the desired LAA orifice location determined by medical expert. The results show that in most cases the desired orifice location is either the location proposed by our method, or a location very close to our proposed location.

4. Discussion

In this section we will discuss the comparison of the proposed method to the other published state-of-the-art methods. Additionally, we will give the practical implementation details of our proposed method and the reasoning behind certain choices of fixed parameter values.

4.1. Comparison to the state of the art

In addition to the direct comparison of the proposed method to the ground truth segmentations, we have compared the proposed method to two methods by Zheng et al. (SIE-PMB [20] and SIE-MRG [21] from Siemens Corporate Technology, Princeton, NJ, USA – SIE) on 20 datasets used in the Left Atrial Segmentation Challenge (LASC) [37]. The resulting segmentations were delineated from the LA by a plane determined by our medical expert. The SIE methods obtain the average dice overlap of 89.59% between themselves, while our method obtains the average dice overlap of 86.58% and 86.26% against the SIE-PMB and SIE-MRG, respectively. Fig. 15 shows the comparison of the segmentation results. Two of the SIE segmentation results in the LASC dataset had a part of the LAA removed during the result standardization for LASC challenge (Fig. 15e and f), affecting our dice overlap to their results negatively. If we remove those two datasets from the evaluation, the average dice overlap between the SIE methods is 88.93%, while our method obtains the average dice overlap of 87.29% and 86.95% against the SIE-PMB and SIE-MRG, respectively.

LASC datasets are focused on the left atrium segmentation and the provided ground truth segmentations do not contain the LAA. Consequently, we were unable to compare both our method and the SIE methods to the ground truth LAA segmentations. However, high overlap of our method to the SIE methods suggests that our method can handle images of varying quality levels. The datasets in the LASC challenge were specifically selected to provide a variety of quality levels: 8 high contrast, 15 moderate contrast, 3 low contrast and 4 high noise datasets [37]. To the best of our knowledge, the two SIE methods are the only fully automatic LAA segmentation methods available. The SIE methods are very fast (SIE-MRG executes within 5 s), but require very large training samples (SIE-PMB was trained on 457 cardiac CT datasets). Our proposed method is completely heuristical and does not require any training.

The work proposed by Jin et al. [22] uses the fully convolutional neural networks (FCNs) combined with the 3D conditional random fields to extract the LAA from the manually selected ROI. The method used 150 datasets for training and evaluation and obtained the mean dice overlap of 94.76%, while performing the segmentation in less than 40 s. The method is an improvement over the work by Wang et al. [23], which obtains a slightly higher dice overlap (95.21%), but requires more than 3.5 min of computation time.

4.2. Method implementation details

Our proposed method is robust to threshold value selection used to produce the mask image. From the anatomical perspective, the method will correctly segment the LAA even with a non-optimal threshold. Fig. 14 shows the effect of the threshold selection. The difference in segmentation between our two experts is a direct result of the selected threshold value during the creation of the ground truth images. Depending on the selected threshold value, when the input image has high levels of noise, the resulting mask image can contain holes inside the LA

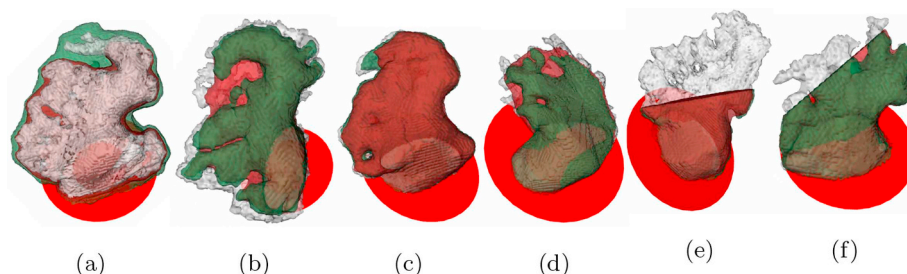


Fig. 15. Segmentation examples from LASC dataset and comparison to SIE-PMB [20] and SIE-MRG [21]. Images show our segmentation result (white), SIE-PMB (red) and SIE-MRG (green).

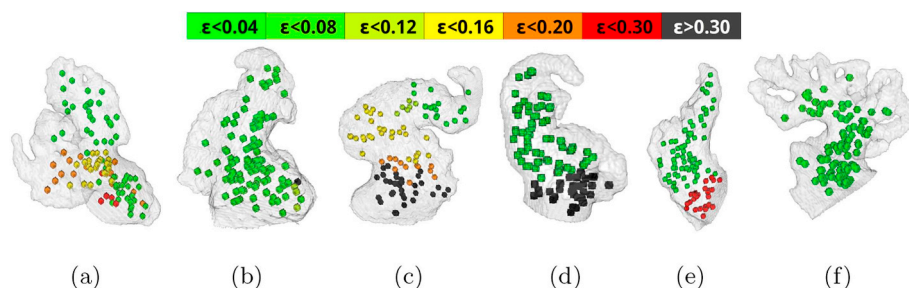


Fig. 16. Visualization of the robustness of the method to seed point selection. Each dot represents a different seed point. The color of the dot represents ϵ – the absolute difference in dice overlap between the segmentation result obtained with that seed point and the ground truth.

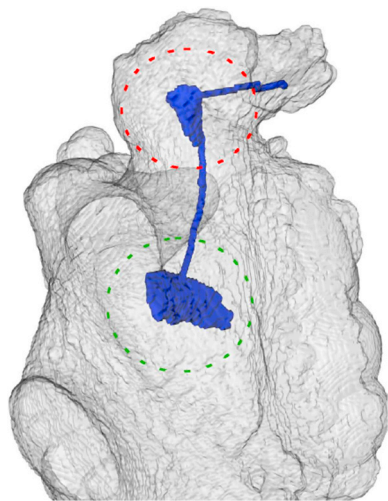


Fig. 17. Clusters of voxels in the maximum radius path during maximum radius tracking. The voxels in the path will cluster at the center of anatomical widenings before continuing the path towards the center of the left atrium. The left atrium itself is among the largest spherical areas in the heart. The tracked path will stay in the LA center until the number of iterations runs out.

near the LAA orifice. The presence of holes in the mask image can introduce errors in the maximum radius tracking step of the method and consequently the localization of the center of the LA. Thus, when working with very noisy images the user should select the threshold value which will minimize the appearance of holes in the mask image near the LAA orifice. The trabeculations inside the LAA do not impair the segmentation results.

The seed point selection is performed with a single click in a desired location in the image. Optimally, the seed point should be placed deep in the LAA, near the tip. We have evaluated the robustness to the seed point selection by segmenting each dataset with a hundred randomly selected seed points (1700 evaluations). The method achieves an average dice overlap of 87.74% and 86.96% against the first and the second expert across all 1700 evaluations. Fig. 16 clearly shows how the distance of the seed point from the orifice affects the segmentation results. The dice overlap achieved in this test is relatively high, even though a large proportion of the randomly chosen seed points are very close to the orifice. When we ignore the half of the seed points closest to the orifice (obviously incorrectly placed seed points), the average dice overlaps with ground truths increase to 90.89% and 90.23%. If the seed point is chosen too close to the atrium, it could happen that only a smaller part of the appendage is segmented because the residual part of the appendage may be too large (in comparison to the initial segmentation) to be added to the final segmentation (see the segmentation refinement step in Subsection 2.7). However, selecting any seed point in the deeper part of the appendage will result in the correct segmentation.

The method for tracking maximum radii voxels (described in Subsection 2.3.1) performs the search for the highest radius voxel in the volume of the maximum inscribed spheres of all previously tracked voxels. Our experiments have shown that using the 26-neighborhood instead of the full spherical neighborhood improves the performance of the method. The method is performed in a predefined number of iterations (estimated from the image size, image spacing and expected anatomical properties of the LAA) in which we are certain that the output set T will contain voxels from the central part of the atrium. The number of iterations in our experiments is set to 4000 (which is larger than needed). In most of our datasets the method detects the correct atrium location in well below 1000 iterations, while only two datasets take up to 1500 iterations. The two examples that need the most iterations have a large spherical widening in the anatomy. One of them is presented in Fig. 17, with the output set T in blue. The voxels in T will cluster in the center of such spherical widening, until the next voxel with the largest radius is the voxel that will continue the path towards the left atrium. Red and green dashed circles in the figure show two largest spherical areas along the path, one in the LAA (red) and the other in the LA (green). The voxels in the red circle will be discarded during centerline extraction (see also Fig. 3b). The center of the LA is extracted from the green cluster by finding the voxel with the largest radius value and discarding all voxels added to T after that voxel. One possible limitation of our method is the case when the LAA has a large spherical part (similar to Fig. 17), but has a narrow neck. There is a possibility that the tracking method will run out of iterations before the path T enters the left atrium, thus failing to detect the centerline properly. In this case we can allow the user to fix the detection by manually selecting the second seed point inside the atrium, as shown in our earlier work [30].

The search for the smallest cross-sectional area along the appendage centerline is not performed along the whole centerline. At the point where the centerline enters the atrium, the area significantly increases and varies due to the shape of the atrium and its connected structures (vessels). In order to avoid the unneeded analysis of the cross-sections in the atrium (to improve speed and accuracy of the computation), we define here criteria for choosing the centerline position at which we stop the search for the minimal area. We observed that the maximum radius inside the LA is always at least twice as large as the radius anywhere inside the LAA. Therefore, we stop the search for minimal areas when the radius along the centerline becomes larger than half of the maximum radius in the atrium. The right side of Fig. 14 shows the plot of calculated areas $a(i)$ and radius weighted rising slopes $w_r(i)$ for the visualized segmentation.

5. Conclusion

We designed an effective semi-automatic method for segmentation of LAA from 3D coronary CT angiography (CCTA) images and a novel orifice localization method to aid the occluder placement procedure. The method requires two inputs from the user: a threshold value and a seed point inside the LAA. The proposed segmentation method is robust

to segmentation leaks. We introduced an approach for extraction of LAA centerline, which is used in the further segmentation steps. Based on the extracted centerline, we introduced a new method for localization of LAA orifice as the proposed location for placement of the occluder device. The segmentation results were evaluated on ground truth images from 17 CCTA datasets created by two medical experts. The obtained Dice coefficient values indicate high correspondence to ground truth segmentations. Our results on proposed locations for the LAA occluder placement (orifice localization) show high correlation to the preferred placement locations determined by a medical expert. The proposed methods yield clinically acceptable results which indicate potential for use in the occluder placement procedure planning. The designed application performs LAA measurements needed to determine the appropriate size of the closure device while requiring little manual intervention to perform the segmentation and analysis.

Compliance with ethical standards

Conflicts of interest

The authors declare that they have no conflict of interest.

Ethical approval

For this type of study, formal consent is not required.

Informed consent

Informed consent was obtained from all individual participants included in the study.

Acknowledgments

This work has been supported in part by Croatian Science Foundation under the project UIP-2017-05-4968.

References

- [1] World Health Organization, *The Top 10 Causes of Death Worldwide Fact Sheet*, Tech. rep. (2017).
- [2] M. Korhonen, A. Muuronen, O. Arponen, P. Mustonen, M. Hedman, P. Jäkälä, R. Vanninen, M. Taina, Left atrial appendage morphology in patients with suspected cardiogenic stroke without known atrial fibrillation, *PLoS One* 10 (3) (2015) e0118822, <https://doi.org/10.1371/journal.pone.0118822>.
- [3] L.P. Budge, K.M. Shaffer, J.R. Moorman, D.E. Lake, J.D. Ferguson, J.M. Mangrum, Analysis of in vivo left atrial appendage morphology in patients with atrial fibrillation: a direct comparison of transesophageal echocardiography, planar cardiac CT, and segmented three-dimensional cardiac CT, *J. Intervent. Card Electrophysiol.* 23 (2) (2008) 87–93, <https://doi.org/10.1007/s10840-008-9281-7>.
- [4] J.L. Blackshear, J.A. Odell, Appendage obliteration to reduce stroke in cardiac surgical patients with atrial fibrillation, *Ann. Thorac. Surg.* 61 (2) (1996) 755–759, [https://doi.org/10.1016/0003-4975\(95\)00887-X](https://doi.org/10.1016/0003-4975(95)00887-X).
- [5] M.E. Goldman, L.A. Pearce, R.G. Hart, M. Zabalgoitia, R.W. Asinger, R. Safford, J.L. Halperin, S. P. i. A. F. Investigators, et al., Pathophysiologic correlates of thromboembolism in nonvalvular atrial fibrillation: I. Reduced flow velocity in the left atrial appendage (The Stroke Prevention in Atrial Fibrillation [SPAF-III] study), *J. Am. Soc. Echocardiogr.* 12 (12) (1999) 1080–1087.
- [6] S.S. Chugh, R. Havmoeller, K. Narayanan, D. Singh, M. Rienstra, E.J. Benjamin, R.F. Gillum, Y.-H. Kim, J.H. McAnulty, Z.-J. Zheng, M.H. Forouzanfar, M. Naghavi, G.A. Mensah, M. Ezzati, C.J.L. Murray, Worldwide epidemiology of atrial fibrillation: a global burden of disease 2010 study, *Circulation* (2013), <https://doi.org/10.1161/CIRCULATIONAHA.113.005119> CIRCULATIONAHA.113.005119.
- [7] S. Panaich, J. Holmes, R. David, Left Atrial Appendage Occlusion, (2017).
- [8] J. Holmes, R. David, S.K. Doshi, S. Kar, M.J. Price, J.M. Sanchez, H. Sievert, M. Valderrabano, V.Y. Reddy, Left atrial appendage closure as an alternative to warfarin for stroke prevention in atrial FibrillationA patient-level meta-analysis, *J. Am. Coll. Cardiol.* 65 (24) (2015) 2614–2623, <https://doi.org/10.1016/j.jacc.2015.04.025>.
- [9] V.Y. Reddy, S. Möbius-Winkler, M.A. Miller, P. Neuzil, G. Schuler, J. Wiebe, P. Sick, H. Sievert, Left atrial appendage closure with the watchman device in patients with a contraindication for oral anticoagulation, *J. Am. Coll. Cardiol.* 61 (25) (2013) 2551–2556, <https://doi.org/10.1016/j.jacc.2013.03.035>.
- [10] J. Saw, P. Fahmy, R. Spencer, R. Prakash, P. McLaughlin, S. Nicolou, M. Tsang, Comparing measurements of CT angiography, TEE, and fluoroscopy of the left atrial appendage for percutaneous closure, *J. Cardiovasc. Electrophysiol.* 27 (4) (2016) 414–422, <https://doi.org/10.1111/jce.12909>.
- [11] O. Goitein, N. Fink, I. Hay, E.D. Segni, V. Guetta, D. Goitein, Y. Brodov, E. Konen, M. Glikson, Cardiac CT Angiography (CCTA) predicts left atrial appendage occluder device size and procedure outcome, *Int. J. Cardiovasc. Imag.* 33 (5) (2017) 739–747, <https://doi.org/10.1007/s10554-016-1050-6>.
- [12] N.C. Wunderlich, R. Beigel, M.J. Swaans, S.Y. Ho, R.J. Siegel, Percutaneous interventions for left atrial appendage exclusion, *JACC (J. Am. Coll. Cardiol.): Cardiovasc. Imag.* 8 (4) (2015) 472–488, <https://doi.org/10.1016/j.jcmg.2015.02.002>.
- [13] J.A. Cabrera, F. Saremi, D. Sánchez-Quintana, Left atrial appendage: anatomy and imaging landmarks pertinent to percutaneous transcatheter occlusion, *Heart* 100 (20) (2014) 1636–1650, <https://doi.org/10.1136/heartjnl-2013-304464>.
- [14] H. Song, Q. Zhou, Q. Deng, J. Chen, L. Zhang, T. Tan, R. Guo, Morphologic assessment of the left atrial appendage in patients with atrial fibrillation by gray values-inverted volume-rendered imaging of three-dimensional transesophageal echocardiography: a comparative study with computed tomography, *J. Am. Soc. Echocardiogr.* 29 (11) (2016) 1100–1108, <https://doi.org/10.1016/j.echo.2016.08.003>.
- [15] J.M. Otton, R. Spina, R. Sulas, R.N. Subbiah, N. Jacobs, D.W.M. Muller, B. Gunalingam, Left atrial appendage closure guided by personalized 3D-printed cardiac reconstruction, *JACC Cardiovasc. Interv.* 8 (7) (2015) 1004–1006, <https://doi.org/10.1016/j.jcin.2015.03.015>.
- [16] V. Caselles, R. Kimmel, G. Sapiro, Geodesic active contours, *Int. J. Comput. Vis.* 22 (1) (1997) 61–79.
- [17] P.A. Yushkevich, J. Piven, H.C. Hazlett, R.G. Smith, S. Ho, J.C. Gee, G. Gerig, User-guided 3D active contour segmentation of anatomical structures: significantly improved efficiency and reliability, *Neuroimage* 31 (3) (2006) 1116–1128, <https://doi.org/10.1016/j.neuroimage.2006.01.015>.
- [18] D. Babin, A. Pizurica, R. Bellens, J. De Bock, Y. Shang, B. Goossens, E. Vansteenkiste, W. Philips, Generalized pixel profiling and comparative segmentation with application to arteriovenous malformation segmentation, *Med. Image Anal.* 16 (5) (2012) 991–1002, <https://doi.org/10.1016/j.media.2012.02.006> wOS:000306390300005.
- [19] D. Babin, A. Pižurica, J.D. Vlyder, E. Vansteenkiste, W. Philips, Brain blood vessel segmentation using line-shaped profiles, *Phys. Med. Biol.* 58 (22) (2013) 8041, <https://doi.org/10.1088/0031-9155/58/22/8041>.
- [20] Y. Zheng, A. Barbu, B. Georgescu, M. Scheuring, D. Comaniciu, Four-chamber heart modeling and automatic segmentation for 3-D cardiac CT volumes using marginal space learning and steerable features, *IEEE Trans. Med. Imag.* 27 (11) (2008) 1668–1681, <https://doi.org/10.1109/TMI.2008.2004421>.
- [21] Y. Zheng, D. Yang, M. John, D. Comaniciu, Multi-part modeling and segmentation of left atrium in C-arm CT for image-guided ablation of atrial fibrillation, *IEEE Trans. Med. Imag.* 33 (2) (2014) 318–331.
- [22] C. Jin, J. Feng, L. Wang, J. Liu, H. Yu, J. Lu, J. Zhou, Left atrial appendage segmentation using fully convolutional neural networks and modified three-dimensional conditional random fields, *IEEE J. Biomed. Health Inf.* 99 (2018), <https://doi.org/10.1109/JBHI.2018.2794552> 1–1.
- [23] L. Wang, J. Feng, C. Jin, J. Lu, J. Zhou, Left atrial appendage segmentation based on ranking 2-D segmentation proposals, *Statistical Atlases and Computational Models of the Heart. Imaging and Modelling Challenges*, Springer, Cham, 2016, pp. 21–29, https://doi.org/10.1007/978-3-319-52718-5_3.
- [24] C. Jin, H. Yu, J. Feng, L. Wang, J. Lu, J. Zhou, Left atrial appendage neck modeling for closure surgery, *Statistical Atlases and Computational Models of the Heart. ACDC and MMWHS Challenges, Lecture Notes in Computer Science*, Springer, Cham, 2017, pp. 32–41, https://doi.org/10.1007/978-3-319-75541-0_4.
- [25] C. Jin, J. Feng, L. Wang, H. Yu, J. Liu, J. Lu, J. Zhou, Left atrial appendage segmentation and quantitative assisted diagnosis of atrial fibrillation based on fusion of temporal-spatial information, *Comput. Biol. Med.* 96 (2018) 52–68, <https://doi.org/10.1016/j.combiomed.2018.03.002>.
- [26] P. Grasland-Mongrain, Segmentation of the Left Atrial Appendage from 3D Images, Ph.D. thesis, Master Thesis ENS Cachan, 2009.
- [27] P. Grasland-Mongrain, J. Peters, O. Ecabert, Combination of shape-constrained and inflation deformable models with application to the segmentation of the left atrial appendage, *Biomedical Imaging: from Nano to Macro, 2010 IEEE International Symposium on, IEEE, 2010*, pp. 428–431.
- [28] H. Zhong, Y. Zheng, G. Funka-Lea, F. Vega-Higuera, Segmentation and removal of pulmonary arteries, veins and left atrial appendage for visualizing coronary and bypass arteries, *Computer Vision and Pattern Recognition Workshops (CVPRW), 2012 IEEE Computer Society Conference on, IEEE, 2012*, pp. 24–30.
- [29] H. Zhong, Y. Zheng, G. Funka-Lea, F. Vega-Higuera, Automatic heart isolation in 3D CT images, *Medical Computer Vision. Recognition Techniques and Applications in Medical Imaging*, Springer, 2013, pp. 165–180.
- [30] H. Leventić, D. Babin, L. Velicki, I. Galić, V. Zlokolica, Semi-automatic left atrial appendage segmentation from 3D CCTA images, *Proceedings ELMAR-2017, IEEE, Zadar, Croatia, 2017*, pp. 39–42.
- [31] C.R. Maurer Jr., R. Qi, V. Raghavan, A linear time algorithm for computing exact euclidean distance transforms of binary images in arbitrary dimensions, *IEEE Trans. Pattern Anal. Mach. Intell.* 25 (2) (2003) 265–270, <https://doi.org/10.1109/TPAMI.2003.1177156>.
- [32] B. C. Lowekamp, D. T. Chen, L. Ibáñez, D. Blezek, The design of SimpleITK, *Front. Neuroinf.* 7. <https://doi.org/10.3389/fninf.2013.00045>.
- [33] D. Babin, A. Pižurica, L. Velicki, V. Matić, I. Galić, H. Leventić, V. Zlokolica, W. Philips, Skeletonization method for vessel delineation of arteriovenous malformation, *Comput. Biol. Med.* 93 (2018) 93–105, <https://doi.org/10.1016/j.combiomed.2017.12.011>.

- [34] E.W. Dijkstra, A note on two problems in connexion with graphs, *Numer. Math.* 1 (1) (1959) 269–271, <https://doi.org/10.1007/BF01386390>.
- [35] D.T. Walker, J.A. Humphries, K.P. Phillips, Anatomical analysis of the left atrial appendage using segmented, three-dimensional cardiac CT: a comparison of patients with paroxysmal and persistent forms of atrial fibrillation, *J. Intervent. Card Electrophysiol.* 34 (2) (2012) 173–179, <https://doi.org/10.1007/s10840-011-9638-1>.
- [36] L. Christiaens, N. Varroud-Vial, P. Ardilouze, S. Ragot, J. Mergy, B. Bonnet, D. Herpin, J. Allal, Real three-dimensional assessment of left atrial and left atrial appendage volumes by 64-slice spiral computed tomography in individuals with or without cardiovascular disease, *Int. J. Cardiol.* 140 (2) (2010) 189–196, <https://doi.org/10.1016/j.ijcard.2008.11.055>.
- [37] C. Tobon-Gomez, A.J. Geers, J. Peters, J. Weese, K. Pinto, R. Karim, M. Ammar, A. Daoudi, J. Margeta, Z. Sandoval, B. Stender, Y. Zheng, M.A. Zuluaga, J. Betancur, N. Ayache, M.A. Chikh, J. Dillenseger, B.M. Kelm, S. Mahmoudi, S. Ourselin, A. Schlaefer, T. Schaeffter, R. Razavi, K.S. Rhode, Benchmark for algorithms segmenting the left atrium from 3D CT and MRI datasets, *IEEE Trans. Med. Imag.* 34 (7) (2015) 1460–1473, <https://doi.org/10.1109/TMI.2015.2398818>.